An Atmospheric Hydraulic Jump in the Santa Barbara Channel

TIMOTHY W. JULIANO AND THOMAS R. PARISH

Department of Atmospheric Science, University of Wyoming, Laramie, Wyoming

DAVID A. RAHN

Department of Geography and Atmospheric Science, University of Kansas, Lawrence, Kansas

DAVID C. LEON

Department of Atmospheric Science, University of Wyoming, Laramie, Wyoming

(Manuscript received 6 December 2016, in final form 8 August 2017)

ABSTRACT

As part of the Precision Atmospheric Marine Boundary Layer Experiment, the University of Wyoming King Air sampled an atmospheric environment conducive to the formation of a hydraulic jump on 24 May 2012 off the coast of California. Strong, northwesterly flow rounded the Point Arguello–Point Conception complex and encountered the remnants of an eddy circulation in the Santa Barbara Channel. The aircraft flew an east–west vertical sawtooth pattern that captured a sharp thinning of the marine boundary layer and the downstream development of a hydraulic jump. In situ observations show a dramatic rise in isentropes and a coincident sudden decrease in wind speeds. Imagery from the Wyoming Cloud Lidar clearly depicts the jump feature via copolarization and depolarization returns. Estimations of MBL depth are used to calculate the upstream Froude number from hydraulic theory. Simulations using the Weather Research and Forecasting Model produced results in agreement with the observations. The innermost domain uses a 900-m horizontal grid spacing and encompasses the transition from supercritical to subcritical flow south of Point Conception. Upstream Froude number estimations from the model compare well to observations. A strongly divergent wind field, consistent with expansion fan dynamics, is present upwind of the hydraulic jump. The model accurately resolves details of the marine boundary layer collapse into the jump. Results from large-eddy simulations show a large increase in the turbulent kinetic energy field coincident with the hydraulic jump.

1. Introduction

The summertime marine boundary layer (MBL) off the California coast is generally characterized by northerly flow. A large region of high sea level pressure over the Pacific Ocean forms under synoptic subsidence and a strong temperature inversion caps the MBL. This inversion marks the boundary between cool, moist air below and warm, dry air above. An area of low pressure resides over the southwestern United States and is associated with a pressure gradient force (PGF) directed toward the east. An attendant horizontal temperature gradient is present because of warmer temperatures over the land and cooler temperatures over the ocean. Accordingly, a thermal wind is present and is oriented from south to north, opposite to the direction of the geostrophic wind.

The MBL top slopes downward from west to east; MBL slopes are enhanced near the shore because of flow around coastal topography (e.g., Koračin and Dorman 2001). Previous studies (e.g., Beardsley et al. 1987; Bridger et al. 1993) suggest that the MBL top ranges from greater than 500 m hundreds of kilometers offshore to roughly 100 m near the coast. More recent observations and numerical simulations have found that the MBL nearly collapses at points along the California coast primarily because of expansion fan dynamics (e.g., Koračin and Dorman 2001; Rahn et al. 2013; Parish et al. 2016a). A southward-directed coastal jet (CJ) with a typical wind speed maximum greater than 25 m s^{-1} sits just below the capping inversion and is strongest where the MBL slope is greatest (e.g., Zemba and Friehe 1987; Parish 2000; Rahn and Parish 2007). Large horizontal and vertical gradients in temperature and water

Corresponding author: Timothy W. Juliano, tjuliano@uwyo.edu

DOI: 10.1175/JAMC-D-16-0396.1

vapor mixing ratio are associated with sloping MBLs. Modeling studies in coastal environments have shown that these gradients perturb the atmospheric refractive index (e.g., Burk and Thompson 1997; Haack and Burk 2001).

Flows around points and capes are traditionally represented by a two-layer shallow water model (e.g., Dorman 1985; Samelson 1992) in which the lower layer is the MBL and the upper layer is the free troposphere. It is usually the case that the MBL depth is lower than the coastal terrain. If the flow around the terrain becomes unbalanced, the adjustment process is determined by the Froude number (Fr). This dimensionless quantity is defined as the ratio of the mean MBL wind speed to the fastest possible gravity wave traveling along the two-layer fluid interface. Mathematically,

$$\mathrm{Fr} = \frac{\overline{U}}{\sqrt{g'H}},$$

where $g' = g(\theta_t - \overline{\theta})/\overline{\theta}$, θ_t is the free troposphere potential temperature, $\overline{\theta}$ is the mean MBL potential temperature (and so $\theta_t - \overline{\theta}$ represents the potential temperature change across the MBL inversion), H is the MBL depth, and $\overline{U}$ is the mean MBL wind speed. A flow characterized by $\mathrm{Fr} < 1$ is considered subcritical, while $\mathrm{Fr} > 1$ is supercritical. When a fluid flow is subcritical, gravity waves are able to propagate upstream in response to the changing coastal terrain. Under supercritical conditions, gravity waves are unable to relay information upstream because the mean flow exceeds the fastest possible gravity wave speed. The transition from supercritical to subcritical flow is necessary for the development of a hydraulic jump.

A hydraulic jump is an abrupt rise in the interface separating two fluid layers. From hydraulic theory, the ratio of the downstream to upstream fluid depths can be derived from continuity and momentum considerations (e.g., Fox et al. 2010) and can be expressed as

$$\frac{h_2}{h_1} = \frac{1}{2}\left(\sqrt{1 + 8\mathrm{Fr}_1^2} - 1\right), \tag{1}$$

where h_1 is the upstream MBL depth, h_2 is the downstream MBL depth, and Fr_1 is the upstream Froude number. This equation shows that the ratio of the fluid depths is solely dependent upon the upstream Froude number, which must be greater than unity for an increase in MBL depth. If Fr_1 is slightly above unity, then an undular hydraulic jump with surface waves may be present. If Fr_1 is much greater than unity, then a roller may form with significant turbulent mixing (Chanson 2009). The mean kinetic energy of the upstream flow must dissipate through either the generation of turbulence or the formation of a stationary gravity wave train that carries the energy downstream (Ball 1956). For instance, a weir may be used to dissipate the kinetic energy of fast-moving flow in an open water channel.

Observations, and to a lesser extent numerical modeling studies, of hydraulic jumps occurring in streams and rivers abound in the literature (e.g., Cummins et al. 2006; Chanson 2009, and references therein). Reports of atmospheric jumps are less common; however, a sizeable body of literature exists in the mountain meteorology community. Jump phenomena in the atmosphere are usually associated with sloping terrain, such as katabatic (e.g., Ball 1956; Lied 1964) and foehn (e.g., Elvidge et al. 2016) flows in Antarctica, the undular morning glory in Australia (e.g., Clarke 1972), and gap flow associated with the Seminoe Mountain chain (Dawson and Marwitz 1982), the Sierra Nevada (e.g., Armi and Mayr 2011), and the Dinaric Alps (e.g., Gohm et al. 2008). Previous work in a marine environment includes oblique hydraulic jumps upstream of Point Sur (Dorman et al. 1999) and Cape Mendocino (Haack et al. 2001). Here we examine a case of a MBL hydraulic jump that occurred downstream of an expansion fan.

2. Data and techniques

The Precision Atmospheric Marine Boundary Layer Experiment (PreAMBLE) was conducted in May and June 2012 with the goal of assessing MBL dynamics using the University of Wyoming King Air (UWKA) platform. The Point Arguello–Point Conception complex and the Santa Barbara Channel (SBC) were target regions for flight operations. This paper focuses on a research flight from 24 May 2012.

Observations during PreAMBLE involved both in situ and remote sensing instrumentation on board the UWKA. A Passive Cavity Aerosol Spectrometer Probe (PCASP-100X) is employed to provide aerosol concentrations (nominally $0.1 \leq D \leq 3.0\,\mu$m; Cai et al. 2013). Also, the Meteorology Research, Inc., universal turbulence indicator is used to measure the eddy dissipation rate (EDR) by relating small-scale turbulence to gust loads on the aircraft (MacCready 1964). Two versions of the Wyoming Cloud Lidar (WCL), one upward-pointing and one downward-pointing, provide important imagery for the present study. The WCL operates at 355 nm and records the backscattered power on co- and cross-polarized channels, and is useful for observing aerosol characteristics and MBL structure. In the MBL, backscattered power returns are strong, while the depolarization ratio is low because of the prevalence of larger, deliquesced aerosols that are inherently spherical. Above the MBL, backscattered power returns are weaker and the

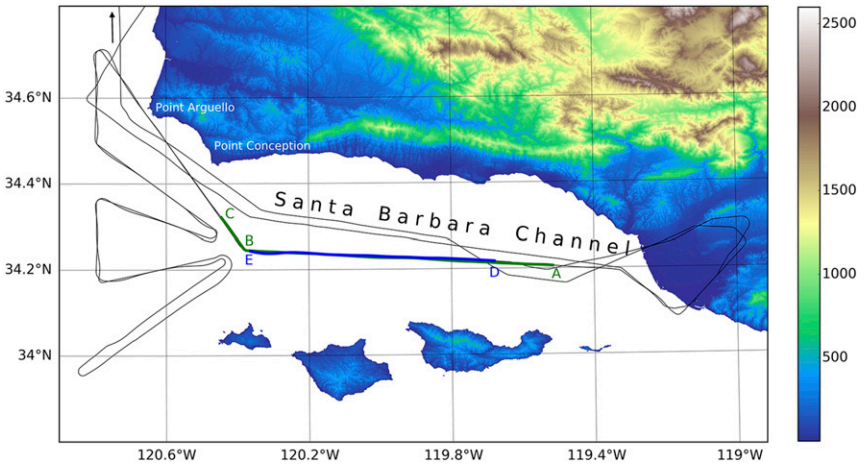

FIG. 1. UWKA flight track (thin black line) from 24 May 2012 operations. Two vertical sawtooth legs are highlighted with thick lines: 2022:35–2042:30 UTC (green; ABC) and 2233:41–2245:45 UTC (blue; DE). Some isobaric flights were conducted farther to the north (denoted by arrow). Terrain elevations are color contoured with scale (m).

depolarization ratio may be higher as a result of smaller, nonspherical particles usually originating from continental sources. A more detailed description of the WCL is available in Wang et al. (2009) and Wang et al. (2012).

PreAMBLE flight strategies included isobaric legs in addition to vertical sawtooth profiles. Here we focus on data obtained exclusively from the latter. Sawtooth flight legs were conducted at two different times on 24 May (Fig. 1). The UWKA traveled from east to west during the first leg (ABC; 2022:35–2042:30 UTC) and from west to east during the second leg (DE; 2233:41–2245:45 UTC).

Differential-GPS techniques (Parish et al. 2007) enable high-fidelity measurement of the height of the aircraft. When combined with accurate measurements of the static pressure, the horizontal pressure gradient can be determined. More recently, D values have been used to complement measurements of the height gradient along isobaric legs in order to provide a two-dimensional view of the pressure field when applied to measurements from vertical sawtooth patterns (Parish et al. 2016b). The D values are the difference between the height of a measured isobaric surface and the height of the same isobaric level in the U.S. Standard Atmosphere as defined by Bellamy (1945). This method allows vertical changes in the horizontal PGF to be depicted.

The field measurements on 24 May are compared with results from simulations using the Weather Research and Forecasting (WRF) Model (version 3.7; Skamarock et al. 2008). A four-domain, one-way nested structure (Fig. 2) is applied to capture synoptic and mesoscale features; $N_x = N_y$ for each domain: N_x = 101, 151, 181, and 211 for d01, d02, d03, and d04, respectively. The outermost domain (d01) has a horizontal grid spacing of 24.3 km and time step of 45 s. Since the grid structure adopts a 3:1 parent grid and time step ratio, the horizontal spacing and time step in the innermost domain (d04) are 900 m and 5/3 s, respectively. There are 84 vertical eta levels; the lowest level is around 19 m MSL and grid points are spaced ~40 m apart in the lowest 1.5 km. The model was run for 30 h beginning at 0000 UTC 24 May 2012.

Model sensitivity to initialization data and planetary boundary layer (PBL) parameterization was tested by comparing the output with UWKA observations. Initialization sources included the 0.5° Global Forecast System (GFS), 12-km North American Mesoscale Forecast System (NAM), and 32-km North American Regional Reanalysis (NARR). PBL parameterizations examined were the Yonsei University (YSU; Hong et al. 2006) and Mellor–Yamada–Janjić (MYJ; Janjić 1994) schemes. The NARR–MYJ combination produced the most reasonable results of the six possible configurations and is used for all model output presented here. See the appendix for more details on the model validation.

NARR assimilates observational data including, but not limited to, radiosondes, surface stations, and satellites. The MYJ PBL parameterization is a 1.5-order, turbulent kinetic energy (TKE) prognostic scheme. Other relevant model configuration options include Lin microphysics (Lin et al. 1983), Betts–Miller–Janjić cumulus (d01 and d02 only; Janjić 1994), Dudhia shortwave radiation (Dudhia 1989), new Goddard longwave (Chou and Suarez 1999), unified Noah land

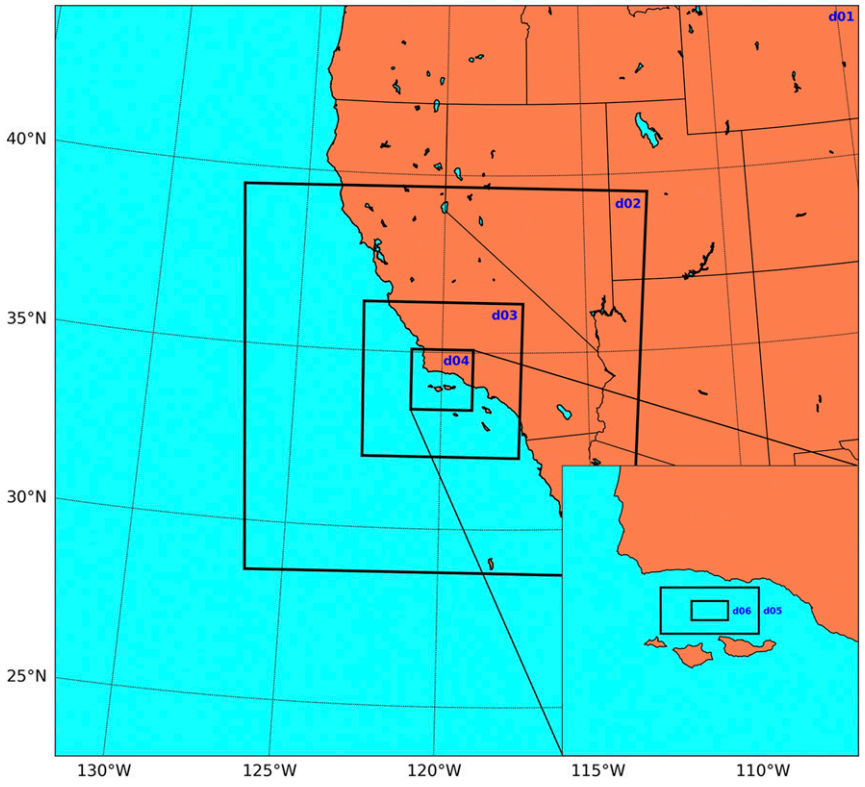

FIG. 2. WRF Model domains. The non-LES simulation used d01–d04, and the LES simulations used d05 or d05 and d06.

surface model (Tewari et al. 2004), and eta similarity scheme (Monin and Obukhov 1954).

Two large-eddy simulations (LESs; Moeng and Sullivan 2015) were conducted with hourly forcing provided by d04 from the NARR–MYJ configuration: a single domain (d05; 300-m horizontal grid spacing) and a two-way nested structure (d05 and d06; 300 and 100 m, respectively) (see Fig. 2). Both runs used the TKE subgrid-scale model option. Thermodynamic and dynamic representation of the MBL and hydraulic jump were similar to that from d04 (900 m) of the non-LES simulation. Therefore, the model results displayed in this paper will be from d04 unless otherwise noted. It is concluded that LESs do not significantly improve model results for this particular case study because of the spatial scale (meso β and meso γ) of the salient features.

When considering numerical model output from an LES domain, TKE may be separated into an unresolved and a resolved portion. The unresolved part is calculated through the subgrid-scale model, while the resolved part is calculated offline. The model output data every 10 s between 1930 and 2030 UTC to allow for an analysis of the TKE associated with the hydraulic jump. This time interval was chosen because an averaging window of at least 30 min is required to calculate the resolved TKE (Schmidli 2013; Wagner et al. 2015). Since the u, v, and w components of the wind are on a regular grid, they are linearly detrended over the 1-h period at each data point. The resolved portion of the instantaneous TKE is calculated as

$$\mathrm{TKE} = \frac{1}{2}\left(\overline{u'^2} + \overline{v'^2} + \overline{w'^2}\right),$$

where u', v', and w' are the perturbation values of the three-dimensional wind components, respectively. These perturbation values are calculated by

$$u' = u - \overline{u},$$
$$v' = v - \overline{v}, \quad \text{and}$$
$$w' = w - \overline{w},$$

where u, v, and w are the instantaneous wind components at each 10-s interval and $\overline{u}$, $\overline{v}$, and $\overline{w}$ are the wind components time averaged over the 1-h period from 1930 to 2030 UTC. The 1-h average of the 10-s deviations are represented by $\overline{u'^2}$, $\overline{v'^2}$, and $\overline{w'^2}$. Total TKE is then simply the addition of the unresolved and resolved TKE.

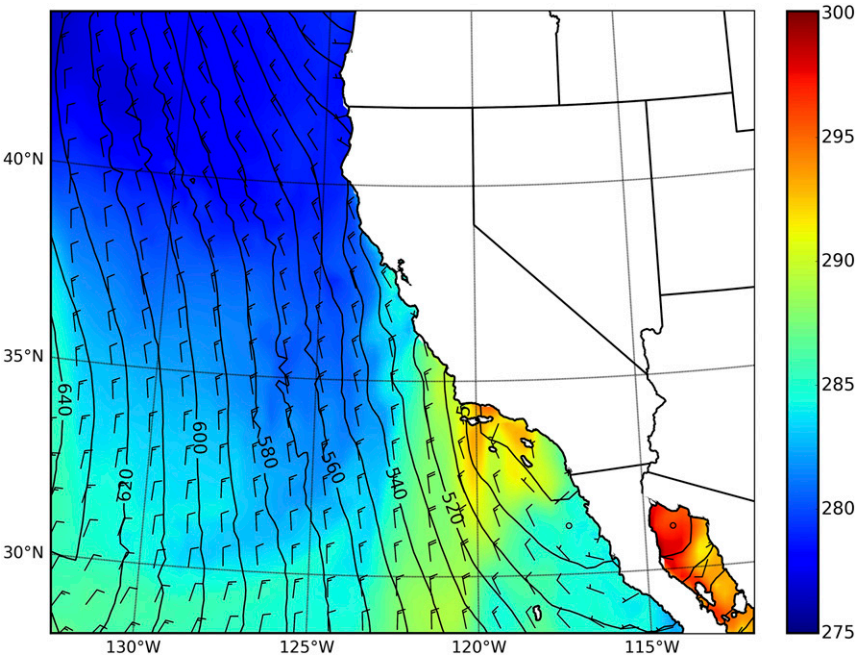

FIG. 3. The 1800 UTC 950-hPa synoptic conditions from NARR–MYJ WRF Model simulation (d01). Variables plotted include wind barbs ($m\,s^{-1}$), geopotential height every 10 m (black solid lines), and temperature (color contoured with scale; K).

3. From synoptic conditions to turbulence: The hydraulic jump

a. Overview

The large-scale meteorological setup on 24 May 2012 is investigated using model output from d01 (Fig. 3). A broad area of high pressure and relatively cool temperatures are present well to the west of the California coast, while a thermal low featuring much warmer temperatures is situated inland. Height contours are oriented north–south offshore with more turning of the wind present near the coastline of Southern California. Winds are from the north-northwest at 10–15 $m\,s^{-1}$ at 950 hPa. Various observational sources report alongshore wind magnitudes greater than 15 $m\,s^{-1}$ on 24 May because of a sea level PGF that is much stronger than the May climatology (Rahn et al. 2016).

Satellite imagery from early in the morning on 24 May (not shown) reveals some patchy marine stratus in the southeastern portion of the SBC propagating to the west. These clouds dissipate by around 1730 UTC; however, they may be remnants of a cyclonic disturbance that developed during the nighttime hours as commonly occurs in the California Bight (Parish et al. 2013). The authors report that eddy circulations in the channel were present on over 70% (24 of 33) of the mornings during the PreAMBLE field campaign. Bosart (1983) provides further discussion on the role of the coastal topography in forming cyclonic eddy circulations in the bight.

b. Airborne observations by the UWKA

Cross sections from the ABC and DE afternoon vertical sawtooth profiles will be examined in this section. All figures display linearly interpolated meteorological fields along with the UWKA flight track. Interpolated UWKA data using the kriging method were also examined (not shown); however, few differences are seen since changing the interpolation method does not overcome the lack of observations between profiles. The distance scale used in Fig. 4 begins at point C (see Fig. 1) during leg ABC to facilitate identification of any spatial movement of the hydraulic jump.

Flight leg ABC captures a robust hydraulic jump in the SBC (Fig. 4a). A significant rise (100–250 m) in the 292–297-K isentropes is seen between about 30- and 40-km distance. Upwind of the jump, isentropes slope downward, suggesting a near collapse of the MBL. Horizontal wind speeds in the CJ are near 23 $m\,s^{-1}$ (not shown). UWKA observations show a remarkable decrease in the u component of the wind downstream, concurrent with the jump. The thermal structure in the air mass to the east features a weaker vertical potential temperature gradient as isentropes slope upward with increasing distance.

Two hours after the hydraulic jump was initially detected, the UWKA headed west along a nearly identical

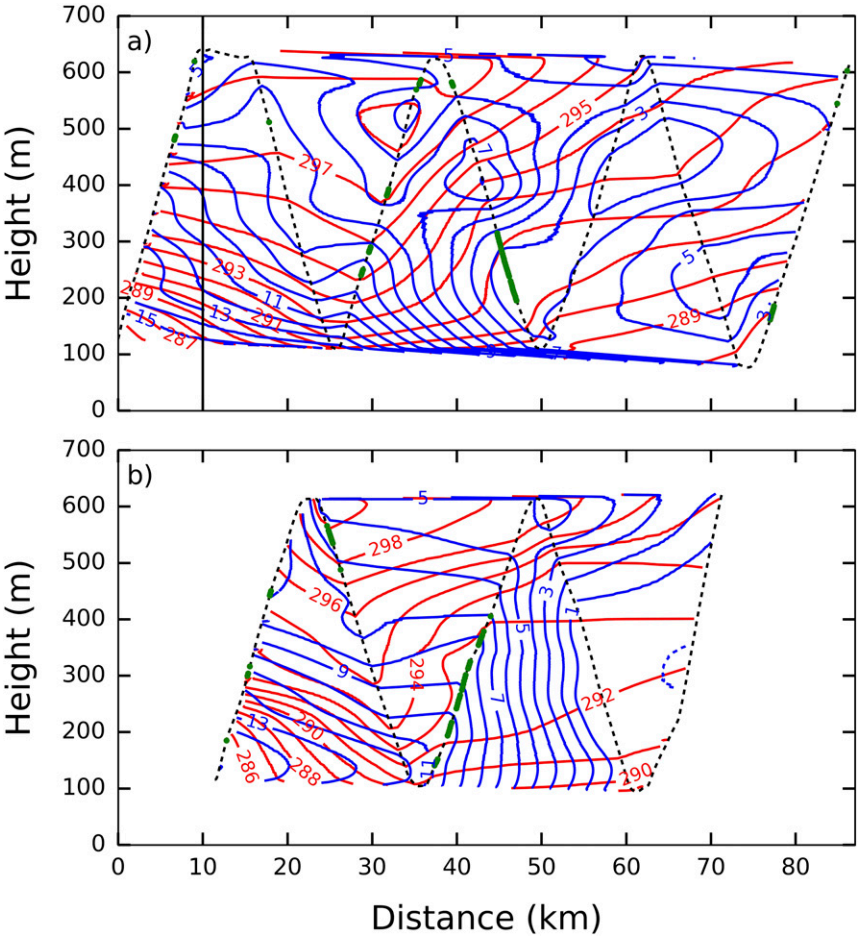

FIG. 4. Interpolated vertical cross section along UWKA flight track (a) ABC and (b) DE in Fig. 1 with potential temperature contoured every 1 K (red solid lines), u component of the wind every 1 m s^{-1} (blue lines), and vertical velocity > 30 cm s^{-1} (green along flight track). Blue solid (dashed) lines indicate a positive (negative) u component. The flight track is also shown (black dashed lines). The vertical black line indicates point B in Fig. 1 where the aircraft changed heading. Northwest is to the left.

track to reveal a similar atmospheric structure: a near collapse upstream into a hydraulic jump followed by a quiescent environment downstream (Fig. 4b). The 293–295-K isentropes rise 200 m over a 10-km distance, but the 292-K theta surface only rises ~50 m. Once again, a strong deceleration in the u component of the wind is seen immediately downwind of the jump. Maximum CJ wind speed values are similar to those measured during leg ABC (not shown). Downstream conditions remain largely unchanged.

Observations show that the jump does have positive vertical velocities (w) associated with the rise in isentropes (Figs. 4a,b). A significant portion of the flight path for transects ABC and DE shows $w > 30\,\text{cm}\,\text{s}^{-1}$ just downstream of the jump. The maximum values of w measured by the UWKA, ~100 and 170 cm s^{-1} for tracks ABC and DE, respectively, increase over time. The area where $w > 30\,\text{cm}\,\text{s}^{-1}$ ranges from about 200 to 400 m MSL and is a bit more extensive in Fig. 4b.

WCL observations, shown in Fig. 5, support the in situ measurements and yield more detail. A clear signal underscores the near collapse of the MBL from 200 to 75 m between distances 0 and 35 km. Near 36-km distance (~2033:45 UTC), lidar returns indicate an extreme rise associated with the MBL top and suggest a hydraulic jump. The abrupt rise, as indicated by the lidar, matches the marked upward trend seen in the isentropes in Fig. 4a. Motions associated with the jump appear to cause vertical mixing between the MBL and the free troposphere. These perturbations seem to be related to the ~(250–700)-m layer downstream of the jump (>40-km distance). The attenuated backscatter reveals a complex, multilayered structure that is present in the eastern portion of the SBC. Moreover, the

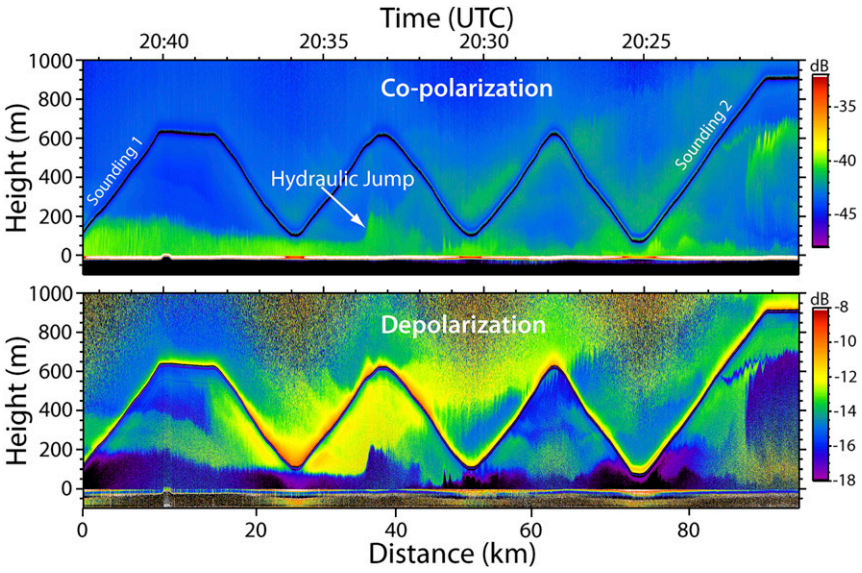

FIG. 5. Copolarization and depolarization from the upward- and downward-pointing WCLs along flight track ABC. The UWKA flight track is shown (black solid line). The distance scale corresponds to that used in Fig. 4. A time scale is also included.

MBL height in the channel varies with distance and is very shallow (~100 m) in some regions.

The MBL depth measured by the lidar may be used to estimate the upstream Froude number Fr_1. From Eq. (1) and using $h_1 = 75$ m and $h_2 = 225$ m, $Fr_1 \approx 2.5$. According to Chanson (2009), the hydraulic jump may resemble an undular jump with some turbulent mixing. Regularly spaced waves along the interface between the MBL and free atmosphere are not evident downstream of the jump. Closer to the jump [~(2029:30–2031:30) UTC], however, less coherent structures are evident that show up as staccato-like rises in the MBL depth. The aforementioned mixing across the MBL top in this region is likely due to small-scale turbulence as the flow transitions from supercritical to subcritical.

About two hours later, WCL imagery along flight track DE (Fig. 6) does not clearly depict a hydraulic jump. According to Fig. 4b, the jump should occur around 40-km distance (i.e., between the strongest rise in isentropes and deceleration in near-surface wind).

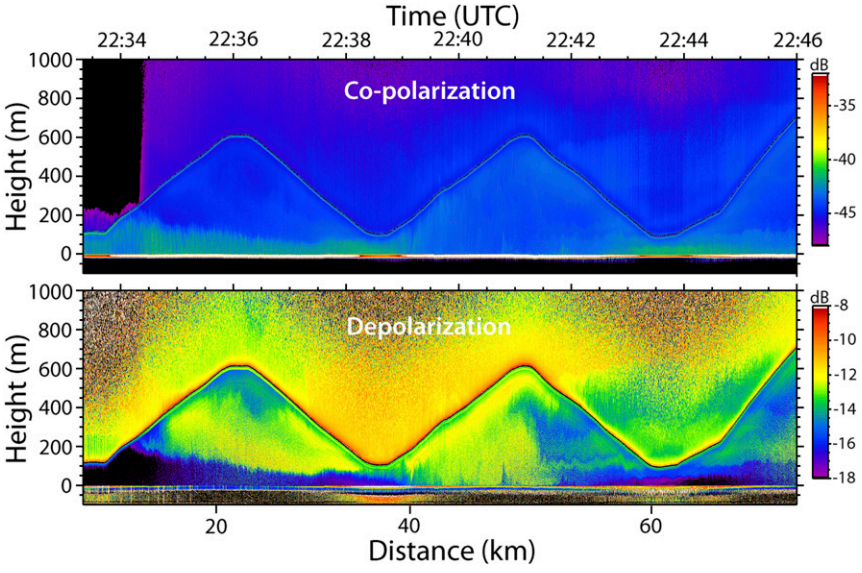

FIG. 6. As in Fig. 5, but along flight track DE.

Instead, a decrease in the copolarization signal and an increase in the depolarization signal near the ocean surface indicates a full MBL collapse at this location. Upstream of the collapse (~30-km distance), the MBL depth is perturbed upward. The cause of this particular feature is unknown. Farther downstream of the collapse, near 50-km distance, wavelike motions in depolarization are evident atop the shallow MBL (~100 m deep).

c. *WRF Model simulation*

Results from the high-resolution numerical simulations are now presented. Simulated 1000-hPa divergence and streamline analyses at 2000 UTC from d04 are shown in Fig. 7a. Upwind of Point Arguello, large values of convergence (magnitudes $> 4 \times 10^{-4}\,s^{-1}$) are consistent with a compression bulge. Around the headlands and just downstream of Point Conception, strong divergence (up to $7 \times 10^{4}\,s^{-1}$) is present, similar to other studies (e.g., Koračin and Dorman 2001). As the flow responds to the bend in the coastal topography, it becomes unbalanced and accelerates down the gradient. Such ageostrophic flow in the bight was ubiquitous during the PreAMBLE campaign (e.g., Rahn et al. 2013; Parish et al. 2014, 2016a; Rahn et al. 2017). Spreading of streamlines in this region is consistent with an expansion fan and linked to the near collapse of the MBL. The location of the hydraulic jump is apparent as a local maximum in convergence (near $5 \times 10^{-4}\,s^{-1}$). This is not surprising considering the observed wind deceleration in Fig. 4a. As depicted by WRF, the UWKA track passed through some of the strongest convergence associated with the jump. An abrupt change in streamlines occurs to the east, concurrent with the SBC air mass, indicating evidence of a weak cyclonic circulation. Above this level, at 925 hPa, northerly offshore continental flow is evident (Fig. 7b). Wind speeds in the lee of Point Conception at this level are $\sim 10\,m\,s^{-1}$ (not shown). Because the topography north of the SBC slopes downward toward the coast, a north wind over the relatively warm land is associated with warm air advection that subsides into the SBC. The combination of warm air advection and adiabatic warming through descent may act to enhance the MBL collapse.

Horizontal convergence near the surface is associated with upward vertical motion through the continuity equation under the assumption of incompressibility. Because the spinup of cyclonic (vertical) vorticity is associated with convergence, its time tendency may be used to diagnose vertical motion. Using WRF output, maximum values of relative vorticity are collocated with the jump feature (not shown). These values range from $\sim 4.4 \times 10^{-3}$ at 1800 UTC to $\sim 4.1 \times 10^{-3}\,s^{-1}$ at 2200 UTC. Since the change in relative vorticity associated with the hydraulic jump over this time period is small, then the spinup of cyclonic vertical vorticity by the horizontal shear zone accounts for only a very small portion of the observed vertical motion. Even if there is an interaction between the northwesterly and southeasterly winds in the bight, the fundamental transition from a supercritical to a subcritical flow regime that leads to rising motion (manifested as a hydraulic jump) does not change.

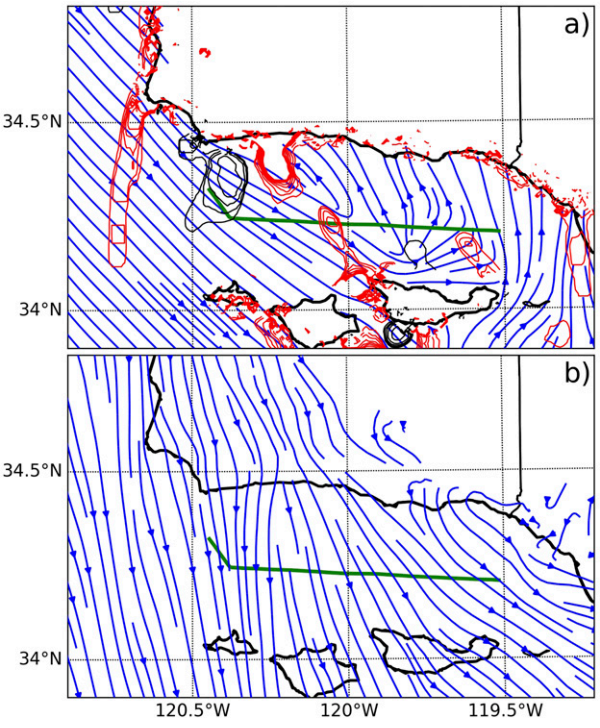

FIG. 7. The 2000 UTC WRF output for d04 of (a) 1000-hPa streamlines (blue solid lines) and divergence (black solid lines) and convergence (red solid lines) every $1 \times 10^{-4}\,s^{-1}$ and (b) 925-hPa streamlines (blue solid lines). Divergence is contoured from 4 to 9 ($\times 10^{-4}\,s^{-1}$), while convergence is contoured from -9 to -2 ($\times 10^{-4}\,s^{-1}$). A nine-point smooth is applied to the divergence field. UWKA flight track ABC is also shown (green solid line).

Cross sections are generated using the UWKA flight track endpoints. For track ABC, two cross sections (C to B and B to A) are stitched together. A hydraulic jump is modeled at 2000 UTC (Fig. 8a). Upstream of the jump, the MBL top, which may be approximated by the 288 K isentrope, transitions from 175 to 75 m in less than 25 km. The sloping MBL leads to a strong CJ, as the u component of the wind reaches $17\,m\,s^{-1}$ (total horizontal wind speed around $23\,m\,s^{-1}$; not shown but consistent with observations). The jump is resolved near 38-km distance, which is only ~2 km different from the location estimated using WCL imagery. A significant decrease in wind speed ($\sim 13\,m\,s^{-1}$ over 10 km) occurs before a transition into the quiescent

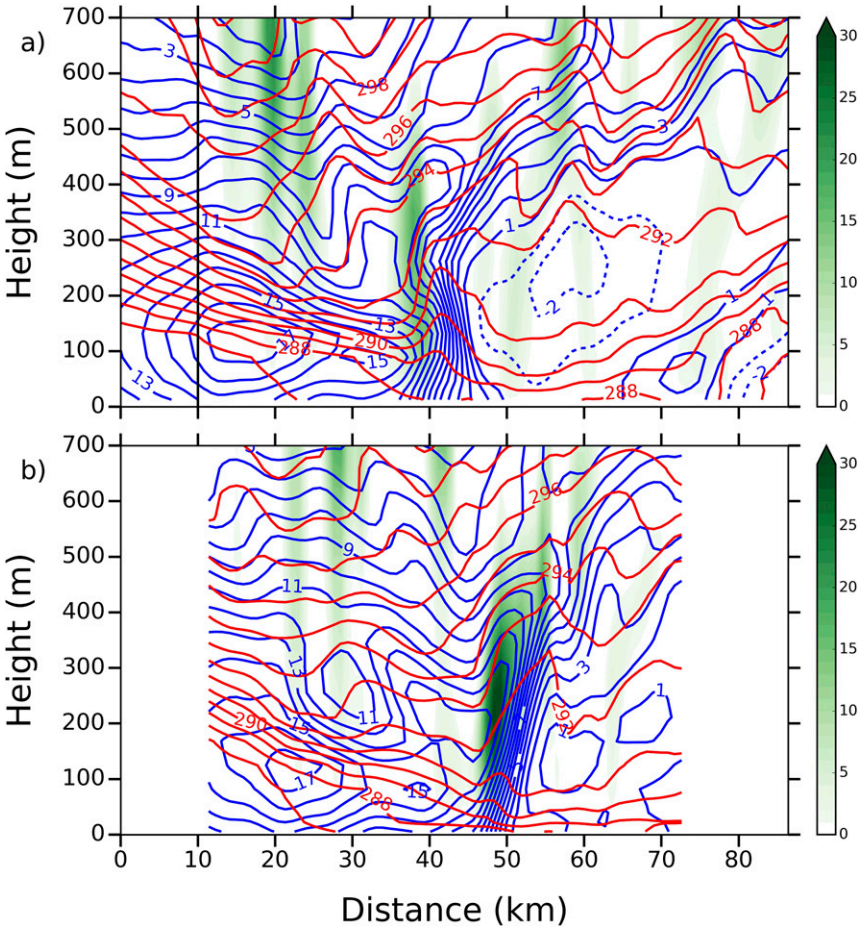

FIG. 8. Model output (d04) along UWKA flight track (a) ABC at 2000 UTC and (b) DE at 2200 UTC with potential temperature contoured every 1 K (red solid lines), u component of the wind every 1 m s^{-1} (blue lines), and vertical velocity (cm s^{-1}; color contoured with scale). Blue solid (dashed) lines indicate a positive (negative) u component. The vertical black line indicates point B in Fig. 1 where the aircraft changed heading. Northwest is to the left.

SBC air mass. Using Fig. 4a to compare, WRF appears to accurately represent the atmospheric environment. Isentropes rise approximately by the same amount in both the observations and numerical simulations. The deceleration in wind speed, however, occurs over a shorter distance in the model, but this may be due to the interpolation of observations between flight legs at low levels (~25-km distance) across the hydraulic jump. Downstream, isentropes slope upward toward the east and the MBL deepens to near 250 m. The model does show a slight easterly component just downwind of the jump near 60-km distance, while the UWKA measured a westerly component in Fig. 4a. WRF also had issues representing the temporal evolution of easterly flow accompanying an eddy in the bight on 3 June 2012 (Rahn et al. 2014).

The 2200 UTC cross section from WRF features a pronounced MBL collapse but a weaker hydraulic jump (Fig. 8b). The jump propagates about 8 km to the east (in the cross-section plane) over two hours, corresponding to a speed of ~1.1 m s^{-1}. Because the cross sections in Fig. 8 are along nearly the same path, the jump feature may be considered quasi-stationary.

Hydraulic jump vertical velocities from d04 are significantly smaller than those measured by the UWKA, but they do match the position of the isentrope rise (Fig. 8). Also, the maximum values represented by d04 increase from 2000 to 2200 UTC (approximately 20–30 cm s^{-1}). The vertical velocity magnitude discrepancy between the observations and the model is not unexpected, as WRF tends to have difficulty in representing sharp vertical gradients that are common in the MBL (e.g., Rahn et al. 2014; Parish et al. 2016a). Moreover, since the jump feature has a limited horizontal extent, sufficient horizontal resolution is needed to minimize the impact of smoothing. Recall that the horizontal grid spacing in d04 is 900 m and the vertical

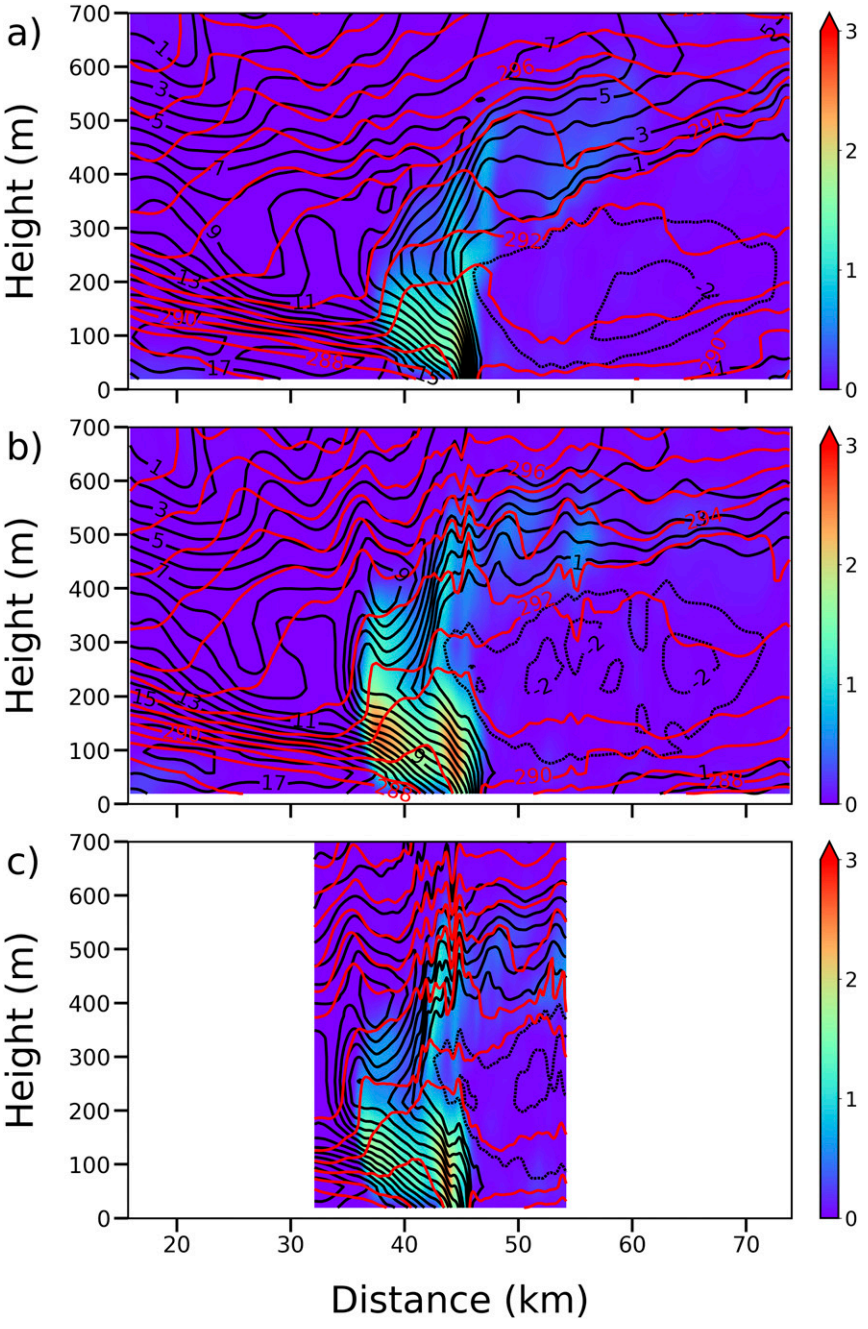

FIG. 9. As in Fig. 8a, but showing LES-resolved potential temperature contoured every 1 K (red solid lines), u component of the wind every 1 m s^{-1} (black solid lines), and TKE (color contoured; m^2 s^{-2}) for (a) single domain simulation (d05), (b) two-way nested simulation (d05), and (c) two-way nested simulation (d06). Contour labels are not included in (c) for clarity. The distance scale corresponds to that used in Fig. 8.

grid spacing at lower levels is ~40 m. Output from d05 and d06 from the two-way nested WRF-LES simulation at 2000 UTC indicate maximum values of w around 56 and 92 cm s^{-1}, respectively, collocated with the jump (not shown). Since the horizontal grid spacing in d05 and d06 is 300 and 100 m, respectively, the higher resolution can more accurately capture the vertical velocity field.

TKE values from d05 and d06 are plotted in Fig. 9. Values within the upstream MBL are minimal, suggesting any shear-driven turbulence produced by the CJ

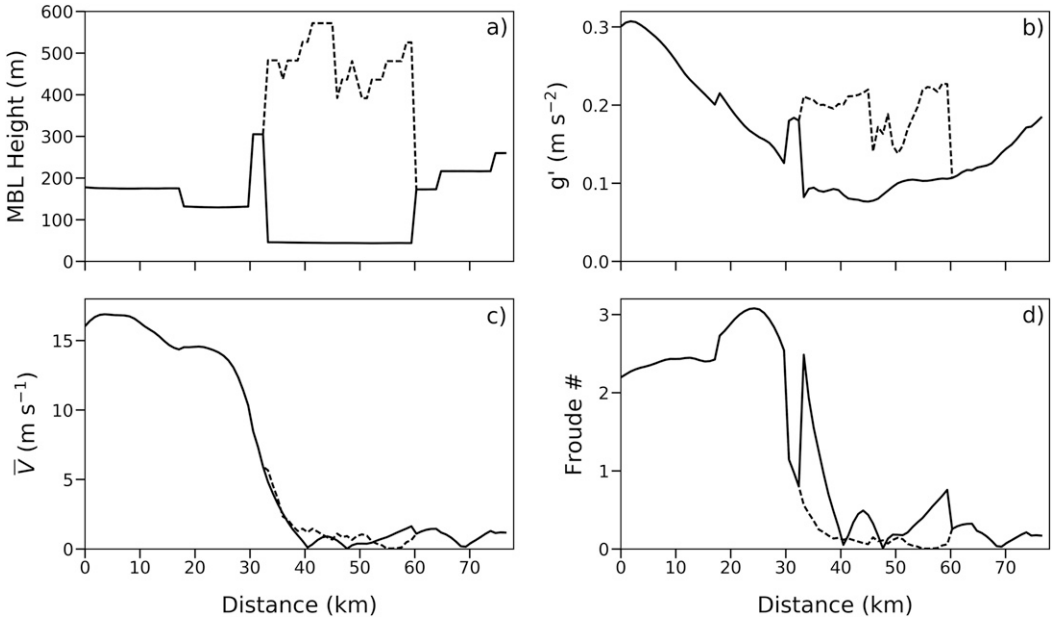

FIG. 10. Calculations of (a) MBL height, (b) g', (c) magnitude of mean MBL wind speed, and (d) Froude number from model output for the cross section in Fig. 8a at 2000 UTC. Distance = 0 km here corresponds to the UWKA heading change at distance = 10 km in Fig. 8a. Solid and dashed lines represent calculations from two different MBL-top detection methods. See the text for more details.

or vertical mixing (entrainment) at the MBL top is quickly dissipated. Kinetic energy of the mean flow is expected to dissipate through turbulence generation by the hydraulic jump, and indeed, the simulations show a broad region of enhanced TKE values beginning at about 36-km distance. There are two main areas of TKE generation. The first area is associated with the strong deceleration of winds below ~200 m MSL and it produces maximum TKE values of ~2.13, ~2.65, and ~2.70 $m^2 s^{-2}$ in Figs. 9a, 9b, and 9c, respectively. The second area accompanies what appears to be high-frequency gravity waves from ~41- to 45-km distance and above ~300 m MSL. These waves are explicitly resolved by d06 and are particularly noticeable in the temperature field in Fig. 9c. Previous studies involving hydraulic jumps in mountainous terrain reveal TKE values ranging from approximately 5 to 10 $m^2 s^{-2}$ (e.g., Gohm et al. 2008; Strauss et al. 2015; Elvidge et al. 2016). While the TKE magnitudes shown here are less, they are reasonable. Overall, the conversion of mean KE to TKE is well represented by the model for this hydraulic jump case.

One important difference between the jump event presented here and those examined in previous reports is that the MBL is thinning and accelerating with a non-sloping (ocean) surface underlying it. Thus, only the MBL top is sloping downward. The primary mechanism responsible for the resultant increase in the Froude number to a supercritical level is expansion fan dynamics. This is in strong contrast to plunging flow over mountainous topography, whereby the flow upstream of the jump accelerates because of the underlying terrain sloping downward. Gravity clearly plays a much more important role in the latter mechanism. Additionally, reports of hydraulic jumps in mountainous regions involve appreciable vertical displacements (>500 m) of the thinning PBL flow upstream of the jump that are neither observed nor modeled in the 24 May 2012 case.

The flow transition in the SBC is investigated using model output from d04. Figure 10 shows the spatial change in the Froude number along the cross section in Fig. 8a from the UWKA heading change and eastward. The individual terms that contribute to Fr are also plotted for reference. The MBL height (Fig. 10a) is determined by taking the lower level of the strongest vertical potential temperature gradient in a layer within the lowest 400 m. Observations (Figs. 4a and 5) and visual inspection of the vertical cross section from WRF (Fig. 8a) indicate that the MBL top is below 400 m for much of the flight track. Between ~41- and 70-km distance in Fig. 8a, however, the strong vertical potential temperature gradients bifurcate. In this region, the MBL height is identified using the method described above (solid line) in addition to applying a constraint that the MBL top must lie between ~125 and 575 m (dashed line). The solid and dashed lines in the remaining panels in Fig. 10 therefore represent the respective calculation using these two

methods. The component of the horizontal wind tangent to the vertical cross section in Fig. 8a is used as the mean wind speed ($\overline{V}$; Fig. 10b). Figure 10c shows reduced gravity parameter g' that is calculated as

$$g' = \frac{\theta_{\mathrm{MBL_{top}}-20\,\mathrm{hPa}} - \theta_{\mathrm{MBL_{top}}}}{\overline{\theta_{\mathrm{MBL}}}}.$$

Model results depict a clear transition from supercritical to subcritical flow around 30-km distance (Fig. 10d). Upwind, a gradual thickness decrease of the MBL to ~125 m is evident with a spike in thickness to ~300 m where the hydraulic jump occurs. This location compares well to a visual inspection of the cross section. The reduced gravity g' decreases upstream, as the potential temperature difference between the two layers decreases. As anticipated, the maximum wind speeds are associated with the modeled CJ. The flow is supercritical upwind as the Froude number ranges between ~2 and 3. These values compare well to the estimated Fr ≈ 2.5 from lidar imagery at about the same time (see Fig. 5). It is no surprise that the maximum in Fr is found where the MBL is thin and wind speeds are large. Downstream of the jump, Fr quickly drops to a subcritical level. Because the MBL structure is nonclassical east of the discontinuity, assessing the MBL height is challenging. In the region from ~31- to 40-km distance, it is apparent that the calculation of Fr is sensitive to the MBL top detection method. Since the first method (solid lines) calculated the strongest vertical gradient in potential temperature to be at $z \approx 45$ m, Fr spikes immediately downstream of the hydraulic jump. Employing the second method (dashed lines) in this same region yields a much smoother flow transition to subcritical levels. Once the MBL wind speeds become sufficiently weak around 40-km distance, Fr is mostly insensitive to the methodology. These results support the idea that enhanced turbulent mixing associated with the jump transition zone creates an ill-defined MBL structure.

d. Contrasting air masses in the SBC

The vertical atmospheric structure within the SBC is known to be horizontally inhomogeneous. For instance, Rahn et al. (2013) and Parish et al. (2014) provide strong evidence for deviation from the classical two-layer system. Lidar imagery and in situ UKWA observations suggest offshore continental flow plays an important role.

Measured vertical profiles (solid lines) from the first afternoon track (ABC) on 24 May confirm that two different air masses are present in the channel (Fig. 11). Corresponding profiles from WRF (dashed lines) are also shown in Figs. 11a and 11b. Upstream (downstream) profiles are traced with blue (red) lines. Observed upstream and downstream profiles correspond with sounding 1 and sounding 2, respectively, as labeled in Fig. 5. The WRF-simulated profiles are taken at 2000 UTC and are calculated from averaging nine vertical profiles (900-m horizontal spacing between each profile). The temperature and wind fields from Fig. 8a are used for the calculations shown here (10.8–18.9-km distance for upstream and 63.9–72.0-km distance for downstream).

The upwind temperature and dewpoint structures represent a typical MBL atmosphere, with the MBL top around 175 m (Fig. 11a). A deep, capping inversion of ~8°C and a decrease in dewpoint of nearly 6°C is measured. The decrease is not entirely linear, with undulations seen between ~250 and 400 m. WRF simulates a slightly shallower and warmer MBL upstream. The dewpoint structure is well represented by the model with the exception of a moist bias from ~400 to 500 m and a dry bias above ~550 m. Wind speeds from the northwest are strong at low levels and decrease quickly above the MBL as the wind veers slightly with height (Fig. 11b). The model has a slightly stronger (weaker) v component below (above) 300 m, but the u component is traced closely. Relatively large values of EDR below 200 m suggest the decay of small-scale turbulence within the MBL and near the MBL top, where turbulent entrainment is expected (Fig. 11c). Additionally, aerosol concentrations slowly increase with height and range from about 125–200 cm^{-3} (Fig. 11d).

Downwind, the vertical profiles differ noticeably. The temperature trace is nearly isothermal and much cooler above ~225 m. A weak temperature inversion is observed around 225 m in addition to a subsidence inversion near 575 m. While WRF does have a warm bias throughout the entire profile, the structure is also nearly isothermal. In addition, the modeled downstream temperature profile is cooler than that upstream above 200 m. Much more moisture is present throughout the profile relative to upwind. A moist bias is seen in the model between about 200 and 450 m. The noticeable temperature and dewpoint biases downstream are likely due to misrepresentation of the dissipating cyclonic circulation in the bight (as discussed in section 3c). Winds are generally weak and increase with height above the MBL. The wind profile backs slightly with height, as the low-level wind direction is from the west before turning toward the southwest. WRF has weaker downstream winds that turn from the southwest to northwest. The EDR is less than that found upwind, especially below 200 m. In situ aerosol measurements from the PCASP in Fig. 11d suggest an air mass with continental influence due to higher particle concentrations (220–340 cm^{-3}). Such measurements are

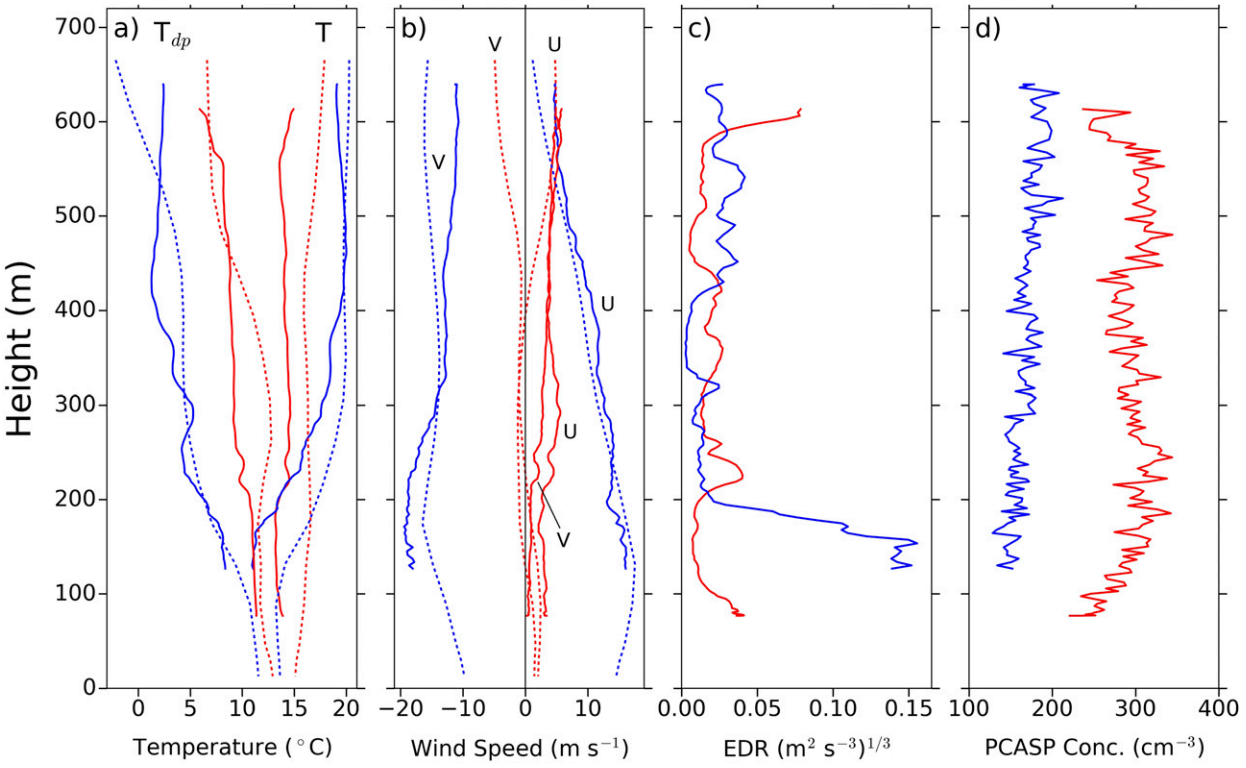

FIG. 11. Vertical profiles of measured (solid lines) and WRF-simulated (dashed lines) (a) temperature and dewpoint and (b) u and v components of wind, as well as measured (c) EDR and (d) PCASP concentration for locations upstream (blue lines) and downstream (red lines) of the hydraulic jump. See the text for more details.

also consistent with the attenuated backscatter observed by the WCL (see Fig. 5).

By definition, whenever the slope of an isobaric surface changes with height, a thermal wind must be present within that layer. This is confirmed through direct calculation of the thermal wind normal to the UWKA flight track using the observed temperature field

$$|V_T| = \frac{R_d}{f} \ln\left(\frac{p_L}{p_U}\right) \nabla_P \overline{T},$$

where p_L and p_U are the lower and upper pressure levels, respectively, and $\nabla_P \overline{T}$ is the horizontal gradient in the mean layer temperature between the lower and upper pressure levels. Here, each layer for which $|V_T|$ is calculated has a thickness of 1 hPa. By definition, the thermal wind is perpendicular to the horizontal temperature gradient with colder air to the left of the thermal wind vector. Upwind of the hydraulic jump, the strongly sloped, low-level isotherms associated with the MBL near collapse, along with a decrease in the horizontal PGF with height, suggest that a southerly thermal wind is present (see Fig. 4a). Downstream of the hydraulic jump, however, the thermodynamic and kinematic states indicate a northerly thermal wind. This analysis suggests that upstream (downstream), the horizontal temperature gradient is directed toward the east (west).

Recall that a horizontal change in D values is akin to a horizontal change in the height of an isobaric surface. After calculating the geostrophic wind from D-value measurements, in addition to reconstructing the geostrophic wind profile through thermal wind inference, Fig. 12a confirms that the atmosphere is in thermal wind balance because the geostrophic wind is constrained by the thermal wind. Flight-normal, low-level geostrophic winds near 40 m s^{-1} upstream contrast strongly with magnitudes of less than 10 m s^{-1} downwind. Upwind, the geostrophic wind quickly decreases with height. Flight-normal components of the horizontal wind indicate ageostrophic environments, both upwind and downwind, that support the idea of downgradient acceleration of the flow. Overall, the upstream flow is much more ageostrophic than the downstream flow.

The thermal wind is explored once again, this time using numerical simulations (Fig. 12b). Both upwind and

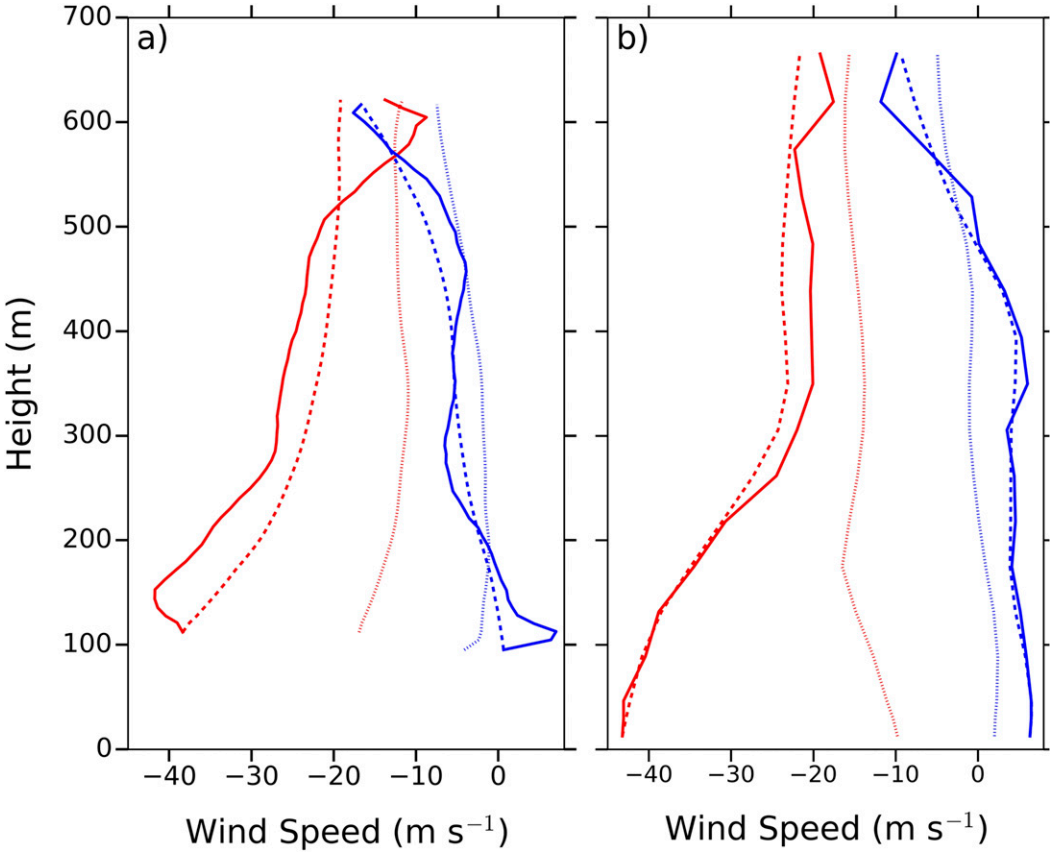

FIG. 12. Vertical profiles from (a) UWKA observations and (b) WRF simulations of the geostrophic wind (solid lines), the geostrophic wind inferred from the thermal wind (dashed), and the measured wind (dotted) for locations upwind (blue lines) and downwind (red lines) of the hydraulic jump. All lines represent the component of the wind normal to the flight leg. The temperature and wind fields from Fig. 4a are used for the calculations shown here (16.0–24.0-km distance for upstream and 54.0–62.0-km distance for downstream).

downwind geostrophic wind profiles are consistent with the observations, and the inferred thermal wind reconstructs the geostrophic profile well. However, less deviation is seen between the geostrophic and thermal wind profiles when compared with measurements, and the upstream flight-normal wind component is a bit weaker below ~175 m.

The contrasting thermodynamic and kinematic fields within the bight are due to the dissipating eddy circulation. In the case examined here, the cyclonic eddy propagated into the channel by the early morning hours and reached a location where the pressure field became adverse for further westward movement. To the east of this location, the horizontal temperature gradient is directed toward the west; this direction is opposite what is typically observed and modeled in the coastal MBL. Thus, the combination of cyclonic wind shear generation downwind of Point Conception and lee troughing due to downslope flow over the coastal terrain form an air mass with both dynamic and thermodynamic characteristics that are different from those usually found in the coastal MBL.

4. Summary and conclusions

Airborne measurements from the PreAMBLE field campaign, along with numerical simulations provided by the WRF Model, captured a hydraulic jump in the SBC on 24 May 2012. Aircraft operations consisted of two vertical sawtooth profiles directed west–east south of Point Conception. A noticeable rise in isentropes mark the location of the hydraulic jump, and the wind quickly decelerates to the east. Lidar signals confirm the presence of the jump feature through a clear increase in the MBL thickness as indicated by backscattered power and depolarization returns. WRF output is consistent with these observations. Cross sections along the UWKA flight legs replicate the jump intensity and location well. Results from WRF-LES show pronounced TKE production in the vicinity of the jump with values ranging from approximately 2 to 3 m^2 s^{-2}.

Strong low-level divergence supports expansion fan dynamics that lead to a near collapse of the MBL upstream of the hydraulic jump. Wind speeds up to $23\,m\,s^{-1}$ in the CJ core are modeled and confirmed through UWKA observations. The flow in this region is supercritical (Fr $>$ 1) because of a combination of the shallow MBL and strong winds. WCL-based estimates of MBL height, using Eq. (1), give an upstream Froude number of ~2.5, while WRF indicates values between ~2 and 3. Farther downstream and east of the jump, model results reveal a clear transition to subcritical (Fr $<$ 1) flow. Remnants of a cyclonic circulation that developed in the early morning hours oppose the mean flow. This air mass has vastly different dynamic and thermodynamic characteristics than the flow rounding the Point Arguello/Point Conception headlands.

Vertical profiles comparing upstream and downstream conditions are mostly consistent between observations and model output. An environment featuring a well-defined MBL and subsidence inversion, in addition to strong northwesterly winds, precedes the hydraulic jump. The model does simulate an upstream MBL that is shallower than that observed. This discrepancy, which may cause a positive bias in the upstream Froude number, may subsequently alter the finescale characteristics of the hydraulic jump (e.g., a taller jump and an increase in TKE generation). East of the jump, the temperature and moisture profiles are nearly uniform, while wind speeds are discernibly weaker and directions vary. The measured *D*-value and temperature fields yield a useful comparison of the geostrophic wind profile and the reconstructed geostrophic wind profile through thermal wind inference. A strong link between the dynamics and thermodynamics is found upstream and downstream of the jump. Downgradient acceleration of the supercritical flow is associated with highly ageostrophic motions. Within the subcritical flow, winds are noticeably less ageostrophic.

During PreAMBLE, expansion fans developed regularly in the general area to the south of Point Conception. A synthesis of all observations during the field campaign revealed that this was the only case for which a clear hydraulic jump was detected (Rahn et al. 2017), but given the frequency of MBL collapses in this region, such jump features may be fairly typical. Positioning of an expansion fan varies depending on specific MBL characteristics such as the wind speed and direction west of Point Arguello, which affects the turning of the wind around Point Conception. In general, the western end of the SBC is where such features were observed.

Abrupt transitions along the boundary between the collapsing MBL and the SBC air mass were commonly observed by the UWKA. Typically, the MBL associated with the expansion fan eroded underneath a deeper, warmer boundary layer found downstream (Rahn et al. 2017). It appears that this day had a particularly well-defined MBL with a strong inversion that extended farther east into the SBC when compared with other days. The shallow MBL seen on many other days during PreAMBLE quickly became diffuse and lost its identity on the downwind side of the expansion fan as heat and momentum mixed vertically. Without a distinct separation of layers, the conceptual model that uses the two-layer hydraulic flow analogy breaks down. In these instances, a hydraulic jump does not form simply because there is no well-defined lower layer.

We propose that two factors are essential to the jump occurrence on this particular day. First, the anomalously strong northwest winds caused a robust MBL thinning and attendant expansion fan leading to a supercritical Fr. Second, a westward-propagating cyclonic circulation in the bight set up a discontinuity between the two flow regimes. The results from this research suggest that the mean flow rounding the coastal bend at Point Conception encountered the SBC air mass that caused an adjustment process and formed a hydraulic jump on 24 May 2012.

Acknowledgments. This research was supported in part by the National Science Foundation through Grants AGS-1034862, AGS-1439515, and AGS-1439594. The authors thank pilots Ahmad Bandini and Brett Wadsworth and scientists Jeff French and Larry Oolman for help with the PreAMBLE field study and UWKA measurements. Additionally, we thank the three anonymous reviewers whose comments have improved the manuscript.

APPENDIX

WRF Model Validation

As described in section 2, six different WRF combinations were selected and simulated for the 24 May 2012 hydraulic jump case. It was concluded that the NARR–MYJ configuration yielded the most accurate results. Justification for this claim is now provided. Data from an isobaric UWKA flight from 1656:30 UTC (34.336285°N, 120.32247°W) to 1703:10 UTC (34.290798°N, 119.96587°W) are compared with WRF output at 1700 UTC along the same flight path (Fig. A1). The mean pressure of the flight leg was ~981 hPa, while the WRF output shown is from the 980-hPa level. UWKA observations (black lines) are linearly interpolated in time (space) to match the grid spacing in d04 (900 m). Output from WRF using the NARR, NAM, and GFS is represented by the red,

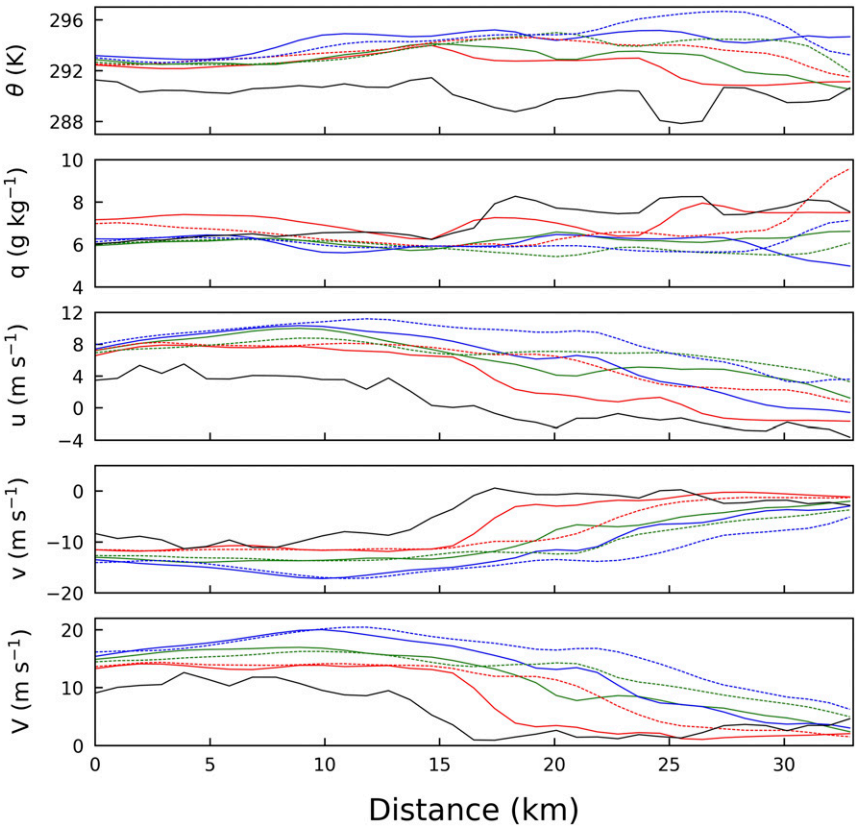

FIG. A1. UWKA observations from ~1656 to 1703 UTC along ~981-hPa isobaric flight track compared with various WRF Model configurations from d04 at 1700 UTC for potential temperature (K), specific humidity (g kg^{-1}), u component of the wind (m s^{-1}), v component of the wind (m s^{-1}), and total horizontal wind speed (m s^{-1}). See the text for details regarding line representation.

green, and blue lines, respectively. The solid (dashed) lines represent the MYJ (YSU) PBL scheme simulations. Both GFS and NAM initializations yielded a significant warm and dry bias in addition to grossly overestimating wind speeds. Also, the MYJ scheme consistently performed better than the YSU scheme. Overall, much better agreement between the observations and model is seen at distances greater than ~15 km, as the UWKA flew from west to east in the SBC. While none of the simulations performed particularly well, clearly the solid, red lines (NARR–MYJ configuration) most closely match the observations. Root-mean-square values for each variable and configuration are shown in Table A1 and confirm this assertion.

TABLE A1. RMSE values for each configuration and variable presented in Fig. A1. The lowest value for each variable is in boldface type.

	θ (K)	q (g kg^{-1})	u (m s^{-1})	v (m s^{-1})	V (m s^{-1})
NARR–MYJ	**2.46**	**0.74**	**3.38**	**3.00**	**3.71**
NAM–MYJ	3.03	1.13	5.83	5.73	6.74
GFS–MYJ	4.44	1.40	5.89	7.65	8.66
NARR–YSU	3.62	1.09	5.35	4.66	5.65
NAM–YSU	3.82	1.58	6.62	6.74	7.82
GFS–YSU	4.72	1.37	8.07	9.11	10.74

REFERENCES

Armi, L., and G. J. Mayr, 2011: The descending stratified flow and internal hydraulic jump in the lee of the Sierras. *J. Appl. Meteor. Climatol.*, **50**, 1995–2011, https://doi.org/10.1175/JAMC-D-10-05005.1.

Ball, F. K., 1956: The theory of strong katabatic winds. *Aust. J. Phys.*, **9**, 373–386, https://doi.org/10.1071/PH560373.

Beardsley, R. C., C. E. Dorman, C. A. Friehe, L. K. Rosenfeld, and C. D. Winant, 1987: Local atmospheric forcing during the Coastal Ocean Dynamics Experiment: 1. A description of the marine boundary layer and atmospheric conditions over a northern California upwelling region. *J. Geophys. Res.*, **92**, 1467–1488, https://doi.org/10.1029/JC092iC02p01467.

Bellamy, J. C., 1945: The use of pressure altitude and altimeter corrections in meteorology. *J. Meteor.*, **2**, 1–78, https://doi.org/10.1175/1520-0469(1945)002<0001:TUOPAA>2.0.CO;2.

Bosart, L. F., 1983: Analysis of a California Catalina eddy. *Mon. Wea. Rev.*, **111**, 1619–1633, https://doi.org/10.1175/1520-0493(1983)111<1619:AOACCE>2.0.CO;2.

Bridger, A. F. C., W. C. Brick, and P. F. Lester, 1993: The structure of the marine inversion layer off the central California coast: Mesoscale conditions. *Mon. Wea. Rev.*, **121**, 335–351, https://doi.org/10.1175/1520-0493(1993)121<0335:TSOTMI>2.0.CO;2.

Burk, S. D., and W. T. Thompson, 1997: Mesoscale modeling of summertime refractive conditions in the Southern California Bight. *J. Appl. Meteor.*, **36**, 22–31, https://doi.org/10.1175/1520-0450(1997)036<0022:MMOSRC>2.0.CO;2.

Cai, Y., J. R. Snider, and P. Wechsler, 2013: Calibration of the passive cavity aerosol spectrometer probe for airborne determination of the size distribution. *Atmos. Meas. Tech.*, **6**, 2349–2358, https://doi.org/10.5194/amt-6-2349-2013.

Chanson, H., 2009: Current knowledge in hydraulic jumps and related phenomena: A survey of experimental results. *Eur. J. Mech. Fluids*, **28B**, 191–210, https://doi.org/10.1016/j.euromechflu.2008.06.004.

Chou, M. D., and M. J. Suarez, 1999: A solar radiation parameterization for atmospheric studies. NASA Tech. Memo. 104606, Vol. 15, 40 pp.

Clarke, R. H., 1972: The morning glory: An atmospheric hydraulic jump. *J. Appl. Meteor.*, **11**, 304–311, https://doi.org/10.1175/1520-0450(1972)011<0304:TMGAAH>2.0.CO;2.

Cummins, P. F., L. Armi, and S. Vagle, 2006: Upstream internal hydraulic jumps. *J. Phys. Oceanogr.*, **36**, 753–769, https://doi.org/10.1175/JPO2894.1.

Dawson, P. J., and J. D. Marwitz, 1982: Wave structures and turbulent features of the winter airflow in southern Wyoming. *Interpretation of Windflow Characteristics from Eolian Landforms*, R. W. Marrs and K. E. Kolm, Eds., GSA Special Papers, Vol. 192, Geological Society of America, 55–64, https://dx.doi.org/10.1130/SPE192-p55.

Dorman, C. E., 1985: Evidence of Kelvin waves in California's marine layer and related eddy generation. *Mon. Wea. Rev.*, **113**, 827–839, https://doi.org/10.1175/1520-0493(1985)113<0827:EOKWIC>2.0.CO;2.

——, D. P. Rogers, W. Nuss, and W. T. Thompson, 1999: Adjustment of the summer marine boundary layer around Point Sur, California. *Mon. Wea. Rev.*, **127**, 2143–2159, https://doi.org/10.1175/1520-0493(1999)127<2143:AOTSMB>2.0.CO;2.

Dudhia, J., 1989: Numerical study of convection observed during the Winter Monsoon Experiment using a mesoscale two-dimensional model. *J. Atmos. Sci.*, **46**, 3077–3107, https://doi.org/10.1175/1520-0469(1989)046<3077:NSOCOD>2.0.CO;2.

Elvidge, A. D., I. A. Renfrew, J. C. King, A. Orr, and T. A. Lachlan-Cope, 2016: Foehn warming distributions in nonlinear and linear flow regimes: A focus on the Antarctic Peninsula. *Quart. J. Roy. Meteor. Soc.*, **142**, 618–631, https://doi.org/10.1002/qj.2489.

Fox, W., P. Pritchard, and A. McDonald, 2010: *Introduction to Fluid Mechanics*. 8th ed. John Wiley & Sons, 754 pp.

Gohm, A., G. J. Mayr, A. Fix, and A. Giez, 2008: On the onset of bora and the formation of rotors and jumps near a mountain gap. *Quart. J. Roy. Meteor. Soc.*, **134**, 21–46, https://doi.org/10.1002/qj.206.

Haack, T., and S. D. Burk, 2001: Summertime marine refractivity conditions along coastal California. *J. Appl. Meteor.*, **40**, 673–687, https://doi.org/10.1175/1520-0450(2001)040<0673:SMRCAC>2.0.CO;2.

——, ——, C. Dorman, and D. Rogers, 2001: Supercritical flow interaction within the Cape Blanco–Cape Mendocino orographic complex. *Mon. Wea. Rev.*, **129**, 688–708, https://doi.org/10.1175/1520-0493(2001)129<0688:SFIWTC>2.0.CO;2.

Hong, S.-Y., Y. Noh, and J. Dudhia, 2006: A new vertical diffusion package with an explicit treatment of entrainment processes. *Mon. Wea. Rev.*, **134**, 2318–2341, https://doi.org/10.1175/MWR3199.1.

Janjić, Z. I., 1994: The step-mountain eta coordinate model: Further developments of the convection, viscous sublayer, and turbulence closure schemes. *Mon. Wea. Rev.*, **122**, 927–945, https://doi.org/10.1175/1520-0493(1994)122<0927:TSMECM>2.0.CO;2.

Koračin, D., and C. E. Dorman, 2001: Marine atmospheric boundary divergence and clouds along California in June 1996. *Mon. Wea. Rev.*, **129**, 2040–2056, https://doi.org/10.1175/1520-0493(2001)129<2040:MABLDA>2.0.CO;2.

Lied, N. T., 1964: Stationary hydraulic jumps in a katabatic flow near Davis, Antarctica, 1961. *Aust. Meteor. Mag.*, **47**, 40–51.

Lin, Y.-L., R. D. Farley, and H. D. Orville, 1983: Bulk parameterization of the snow field in a cloud model. *J. Climate Appl. Meteor.*, **22**, 1065–1092, https://doi.org/10.1175/1520-0450(1983)022<1065:BPOTSF>2.0.CO;2.

MacCready, P. B., Jr., 1964: Standardization of gustiness values from aircraft. *J. Appl. Meteor.*, **3**, 439–449, https://doi.org/10.1175/1520-0450(1964)003<0439:SOGVFA>2.0.CO;2.

Moeng, C. H., and P. P. Sullivan, 2015: Large-eddy simulation. *Encyclopedia of Atmospheric Sciences*, 2nd ed. G. R. North, F. Zhang, and J. Pyle, Eds., Vol. 4, Academic Press, 232–240.

Monin, A. S., and A. M. Obukhov, 1954: Basic laws of turbulent mixing in the surface layer of the atmosphere. *Contrib. Geophys. Inst. Acad. Sci. USSR*, **151**, 163–187.

Parish, T. R., 2000: Forcing of the summertime low-level jet along the California coast. *J. Appl. Meteor.*, **39**, 2421–2433, https://doi.org/10.1175/1520-0450(2000)039<2421:FOTSLL>2.0.CO;2.

——, M. D. Burkhart, and A. R. Rodi, 2007: Determination of the horizontal pressure gradient force using global positioning system on board an instrumented aircraft. *J. Atmos. Oceanic Technol.*, **24**, 521–528, https://doi.org/10.1175/JTECH1986.1.

——, D. A. Rahn, and D. Leon, 2013: Airborne observations of a Catalina eddy. *Mon. Wea. Rev.*, **141**, 3300–3313, https://doi.org/10.1175/MWR-D-13-00029.1.

——, ——, and ——, 2014: Aircraft observations of the marine layer adjustment near Point Arguello, California. *J. Appl. Meteor. Climatol.*, **53**, 970–989, https://doi.org/10.1175/JAMC-D-13-0164.1.

——, ——, and ——, 2016a: Aircraft measurements and numerical simulations of an expansion fan off the California coast. *J. Appl. Meteor. Climatol.*, **55**, 2053–2062, https://doi.org/10.1175/JAMC-D-16-0101.1.

——, ——, and ——, 2016b: Research aircraft determination of D-value cross sections. *J. Atmos. Oceanic Technol.*, **33**, 391–396, https://doi.org/10.1175/JTECH-D-15-0173.1.

Rahn, D. A., and T. R. Parish, 2007: Diagnosis of the forcing and structure of the coastal jet near Cape Mendocino using in situ observations and numerical simulations. *J. Appl. Meteor. Climatol.*, **46**, 1455–1468, https://doi.org/10.1175/JAM2546.1.

——, ——, and D. Leon, 2013: Airborne measurements of coastal jet transition around Point Conception, California. *Mon. Wea. Rev.*, **141**, 3827–3839, https://doi.org/10.1175/MWR-D-13-00030.1.

——, ——, and ——, 2014: Coastal jet adjustment near Point Conception, California, with opposing wind in the bight.

Mon. Wea. Rev., **142**, 1344–1360, https://doi.org/10.1175/MWR-D-13-00177.1.

——, ——, and ——, 2016: Observations of large wind shear above the marine boundary layer near Point Buchon, California. *J. Atmos. Sci.*, **73**, 3059–3077, https://doi.org/10.1175/JAS-D-15-0363.1.

——, ——, and ——, 2017: Synthesis of observations from the Precision Atmospheric Marine Boundary Layer Experiment (PreAMBLE). *Mon. Wea. Rev.*, **145**, 2325–2342, https://doi.org/10.1175/MWR-D-16-0373.1.

Samelson, R. M., 1992: Supercritical marine-layer flow along a smoothly varying coastline. *J. Atmos. Sci.*, **49**, 1571–1584, https://doi.org/10.1175/1520-0469(1992)049<1571:SMLFAA>2.0.CO;2.

Schmidli, J., 2013: Daytime heat transfer processes over mountain terrain. *J. Atmos. Sci.*, **70**, 4041–4066, https://doi.org/10.1175/JAS-D-13-083.1.

Skamarock, W. C., and Coauthors, 2008: A description of the Advanced Research WRF version 3. NCAR Tech. Note NCAR/TN-475+STR, 113 pp., http://dx.doi.org/10.5065/D68S4MVH.

Strauss, L., S. Serafin, S. Haimov, and V. Grubišić, 2015: Turbulence in breaking mountain waves and atmospheric rotors estimated from airborne in situ and Doppler radar measurements. *Quart. J. Roy. Meteor. Soc.*, **141**, 3207–3225, https://doi.org/10.1002/qj.2604.

Tewari, M., and Coauthors, 2004: Implesmentation and verification of the unified Noah land surface model in the WRF model. *20th Conf. on Weather Analysis and Forecasting/16th Conf. on Numerical Weather Prediction*, Seattle, WA, Amer. Meteor. Soc., 14.2A, https://ams.confex.com/ams/pdfpapers/69061.pdf.

Wagner, J. S., A. Gohm, and M. W. Rotach, 2015: The impact of valley geometry on daytime thermally driven flows and vertical transport processes. *Quart. J. Roy. Meteor. Soc.*, **141**, 1780–1794, https://doi.org/10.1002/qj.2481.

Wang, Z., P. Wechsler, W. Kuestner, J. French, A. R. Rodi, B. Glover, M. Burkhart, and D. Lukens, 2009: Wyoming Cloud Lidar: Instrument description and applications. *Opt. Express*, **17**, 13 576–13 587, https://doi.org/10.1364/OE.17.013576.

——, J. French, G. Vali, and P. Wechsler, 2012: Single aircraft integration of remote sensing and in situ sampling for the study of cloud microphysics and dynamics. *Bull. Amer. Meteor. Soc.*, **93**, 653–668, https://doi.org/10.1175/BAMS-D-11-00044.1.

Zemba, J., and C. A. Friehe, 1987: The marine boundary layer jet in the Coastal Ocean Dynamics Experiment. *J. Geophys. Res.*, **92**, 1489–1496, https://doi.org/10.1029/JC092iC02p01489.